Effects of Rigid Body Collisions and Tide-Forced Drift on Large Tabular Icebergs of the Antarctic

D. R. MacAyeal,[1] L. Padman,[2], M. R. Drinkwater,[3] M. Fahnestock,[4] T. T. Gotis, [1] A. L. Gray, [5] B. Kerman,[1] M. Lazzara,[6] E. Rignot,[7] T. Scambos[8] and C. Stearns [6]

Short title: TIDAL DRIFT OF LARGE TABULAR ICEBERGS

Abstract. Following the calving of an iceberg from an ice shelf, many collisions between the new iceberg and the remaining shelf can occur as the iceberg responds to time-varying oceanic and atmospheric forcing. Collisions can cause the iceberg to fracture into smaller pieces, initiate calving of other icebergs from the ice shelf, and can induce a mean drift of the iceberg along the remaining ice front. We investigate the effects of iceberg/ice-shelf and iceberg/iceberg collisions using a model that treats icebergs as finite-sized rigid bodies that respond to ocean tidal forcing. We report a detailed study of the calving and drift of giant tabular icebergs in both the Weddell and Ross Seas of Antarctica which calved between October, 1998, and May, 2000. Model performance is assessed using satellite imagery. An interesting feature of the model is the rectification of an iceberg's tidal motion as a result of collisions. While this feature dominated the model results shown here, it remains to be determined how important tidal processes are relative to non-tidal oceanic and atmospheric processes.

1. Introduction

From October of 1998 to May of 2000, 5 remarkably large icebergs calved from the Ronne and Ross ice shelves of Antarctica (Figures 1 and 2, Table 1) [*Lazzara et al.*, 1999]. These icebergs are among the largest ever to have calved from the Antarctic, and one in particular (B15) may have been the largest iceberg ever witnessed. The total area of these icebergs is ∼32,000 km^2 and they contain ∼4,000 km^3 of ice, which is roughly twice the entire yearly ice accumulation of Antarctica [*Jacobs et al.,* 1992] and is approximately 8 times the annual domestic fresh-water usage in the United States. While much recent attention has been devoted to the loss of ice-shelf area along the Antarctic Peninsula [e.g., *Vaughan and Doake*, 1996; *Skvarca et al.*, 1999; *Scambos et al.*, 2000], the icebergs listed in Table 1 cover ∼3 times as much area as the total shelf lost in the Peninsula region since the mid-1960s [*Lazzara et al.*, 1999].

Figures 1 an

Table 1

Aside from the titanic size of these icebergs, the impact of their calving on the mass balance and long-term areal extent of the Antarctic ice sheet is not remarkable. They appear to represent normal, albeit infrequent events necessary to maintain steady conditions of the Antarctic ice sheet. *Jacobs et al.* [1986] demonstrate from historical maps of ice-front position extending back to 1847 that large-scale calving from the Ross Ice Shelf has been episodic since the time J. C. Ross first explored the region. The historical records suggest that major calving events occur roughly every 50 to 100 years. Between these events, the seaward ice front of the Ross Ice Shelf advances at about the glaciological flow velocity (up to ∼1.1 km a^{-1}). The maps of maximum and

minimum ice-shelf extent displayed by *Jacobs et al.* [1986] suggest that calving of long, sliver-shaped icebergs 30-50 km wide occurs during each major event. This view is supported by the calving events in the Weddell Sea, where calving of A38-A44 between October, 1998 and May, 2000 has restored the front of the Ronne Ice Shelf to a position similar to that observed in the 1950s. The calving of B15-B18 in 2000 may have begun a similar ice-front adjustment process for the Ross Ice Shelf. Presumably, the western half of the Ross Ice Shelf that has yet to calve an iceberg will expel a large iceberg in the near future to complete the process started by B15-B18.

The truly novel feature of the recent large calving events is that they are the first to have been observed closely using satellite-based sensors. We can, therefore, begin a detailed inquiry into how large icebergs are calved, what happens to them after they calve, and how their subsequent drift and break-up influences the marine environment surrounding Antarctica.

In the present study we focus on one particular aspect of iceberg behavior, how intermittent collisions between a nascent iceberg and the remaining parent ice shelf influence an iceberg's initial drift and possible break-up. We further limit our study to iceberg response to ocean tides. Although other time-varying forcing such as wind stress undoubtedly lead to collisions, response to ocean tides is relatively easily modeled and interpreted. The results presented here suggest that ocean tide can be as influential as other oceanic and atmospheric processes while an iceberg remains near (i.e., within $O(10)$ km) to its parent ice front. In particular, we show that tides can transport an iceberg great distances wherever collisions with coasts and ice fronts rectify the iceberg's

otherwise periodic tidal motion.

We refer to the rectification of an iceberg's tidal motion as a "kedging effect", because the motion mimics the similarly named process used by mariners of the 19th century to move large sailing ships when becalmed. An iceberg adrift near an ice shelf front moves along the ice front when the net force associated with the ocean current and sea-surface tilt is "favorable" for motion in some particular direction (i.e., usually westward along the ice front). When the tidal forcing reverses, the iceberg collides with the rigid ice front, where it subsequently becomes anchored and awaits the next favorable tide. With typical tidal forcing of the Ross and Weddell Seas, tidal kedging has the potential to produce tens of kilometers of iceberg transport during the initial post-calving time frame.

One consequence of the many collisions involved in the tidal kedging process described above is the introduction of sudden, powerful stresses within the iceberg that can cause break-up and calving of other icebergs. Frequent collisional contact between A38 and the Ronne Ice Shelf ice front during the 14 days following calving in October, 1998, for example, fractured A38 into many pieces and caused the subsequent calving of A39. Iceberg A39 was originally a promontory forming the western end of the ice-front embayment created by the release of A38. In a similar manner, B15, the massive iceberg in the Ross Sea fractured into several pieces as a result of collisions. It also stimulated the calving of B17, B18 and C16.

Considering the titanic proportions of the pieces of ice involved in collisions associated with the kedging process, and also the massive scale of the subsequent

damage to the ice involved, it is possible to speculate that the impulses associated with iceberg/ice-front collisions may be the largest in nature not involving impacts by extraterrestrial bodies.

2. Satellite Observations

The icebergs studied in this paper are shown at their initial, post-calving locations in Figures 1 and 2. We have used imagery from 4 types satellite sensors to study the post-calving behavior of these icebergs. While little of this imagery is displayed here, the large quantity of satellite data proved to be invaluable to the detailed study of iceberg drift and break-up.

Infrared imagery from the advanced very-high resolution radiometer (AVHRR) facilitated the initial identification of iceberg calving and was most useful for monitoring subsequent day-to-day drift as shown in Figures (3) - (5). The AVHRR imagery is reasonably frequent but can be obscured by cloud cover, limiting tracking of the iceberg positions and geometries. The ∼2-km resolution of AVHRR imagery, while relatively high compared with that of scatterometer and passive microwave imaging discussed below, is rarely sufficient to provide a detailed account of iceberg break-up geometry or to reveal the large rifts at which icebergs and ice shelves tend to fail when undergoing collisions.

Figures (3) -

The problem of cloud cover is overcome by two sensors: the special scanning microwave imager (SSM/I) and various radar scatterometers (such as the European Space Agency's remote sensing satellite ERS-2 C-band radar or the QSCAT Ku-band

radar). Imagery provided by these two sensors is available daily, however the spatial resolution of the images is relatively poor, from ∼5 km to ∼25 km. An example of scatterometer imagery that tracks the location of A38 in the Weddell Sea is provided in Figure 6 [*Drinkwater,* 1998].

Figure 6

By far the most detailed imagery of the icebergs is provided by synthetic aperture radar (SAR) imagery from the Canadian Space Agency's Radarsat satellite and the European Space Agency's ERS-1 and ERS-2 satellites. The spatial resolution of these images is ∼10-20 m. An example of the SAR imagery of A38 several days after break-up (November 3, 1998) is provided in Figure 7. The SAR imagery can, however, be infrequent (e.g., on a monthly interval) and expensive to acquire. We thus rely on SAR imagery in this study only to examine special events, e.g., the break-up patterns of A38 after colliding with the ice front. All routine monitoring of the icebergs is relegated to AVHRR, SSM/I and scatterometer imagery.

Figure 7

Our analysis of satellite imagery is divided into three parts. The first describes identification of precursor rifts in the ice shelves from which the icebergs calved. The second describes the break-up of the original icebergs into smaller pieces soon after calving. The final section describes the subsequent drift of the icebergs (and their pieces) through the time period when the icebergs remained near their parent ice fronts.

2.1. Precursor Rifts and Nascent Icebergs

Large tabular icebergs seem to originate due to the coalescence of giant rifts that cut horizontally across the Antarctic ice shelves [e.g., *Wilson,* 1960]. These rifts are not

the small surface crevasses that are normally encountered on ice sheets and glaciers, but instead cut completely through the ice shelf. The rifts are filled with sea water capped by a melange of multi-year sea ice, snow and ice-shelf pieces [e.g., *Rignot and MacAyeal*, 1998]. The growth of these rifts may be driven by repeated tidal wedging or storm activity.

The precursor rifts that led to the calving of A38, A39, B15 - B18, C16, and A43 and A44 are described in detail by *Lazzara et al.* [1999]. In each calving event, large, long rifts parallel to the ice front eventually link with short rifts extending perpendicular to the ice front. As a result of this pattern, long, narrow icebergs tend to be produced preferentially over more regular shapes. Their large aspect ratio may explain why icebergs tend to be vulnerable to further break-up following calving. The processes responsible for rift extension and link-up, and the speed with which these processes operate, are largely unknown. It is, therefore, not presently possible to forecast large calving events with any useful precision.

2.2. Iceberg Break-up and Sympathetic Calving

The icebergs studied here tended to break into several large pieces and cause other icebergs to calve soon after the original calving event. Iceberg A38 provides the best example of this behavior. When it was first observed emerging from the Ronne Ice Shelf on October 13, 1998 (see inset b in Figure 7), A38 was intact and had rotated by several degrees about its extreme southeast corner. Were it not for this relatively small rotation, the iceberg would have fit exactly within the ice front embayment formed by its calving.

Seven days later (20 October, 1998), the first of 4 images of A38 were acquired using the Radarsat SAR (Figure 7). The sequence of Radarsat images (acquired on October 20, 22 and 27, and November 1, 1998, all at approximately 03:00 UT) show the iceberg moving northwest along the ice front. Images also show that A38 had fractured into three major pieces (labeled A38a, A38b and A38c) and an additional iceberg (A39) was calved, in response to a collision between A38 and the ice front.

The SAR imagery suggests that the original iceberg A38 broke in half because it became wedged between two ice-front contact points at either end, with an unsupported center; and that a horizontal force, either associated with ocean currents or with the forces of the collision, caused the unsupported center to fail. This suggestion is supported by the fact that numerous small pieces were seen to be ejected from the southern side of the original iceberg.

Iceberg B15 in the Ross Sea underwent a similar pattern of events as A38. Shortly after calving, B15's eastern end collided with the ice front east of Roosevelt island, causing B17 and B18 to calve (Figure 4, inset b). Soon thereafter, B15 broke in half as a result of being wedged against the ice front with an unsupported center (Figure 4, inset b). After B15a, the western half of B15 after initial break-up, traversed the length of the ice front, it forced the calving of C16, which was a precarious promontory of ice shelf forming the western end of the ice front.

2.3. Coastal Drift and Collisions

Following calving, AVHRR, SSM/I, scatterometer and SAR imagery was used to track the drifts of A38, A39, B15-18, and A43-44. Summaries of such imagery is provided in Figures 3 - 6. The pattern of drift seen in the imagery is similar to the general patterns noted in previous studies [e.g., *Keys et al.,* 1990; *Gladstone et al.,* in press; *Lichey and Hellmer,* in press], and we refer the reader to these other studies for a general description of iceberg-drift climatology.

Our analysis is distinguished from these other studies by our interest in iceberg-ice front and iceberg-iceberg collisions. As we have said previously, our interest in collisions is motivated by their introduction of forces that influence iceberg drift in a way not previously considered when studying iceberg-drift climatology. The temporal frequencies of AVHRR, SSM/I, scatterometer and SAR imagery of the icebergs in the Ross and Weddell Seas were inadequate, however, to quantitatively assess the number and frequency of such collisions. We therefore rely on indirect evidence of collisions, such as when icebergs were seen touching other icebergs or the ice front, as a means of establishing a qualitative description of the role of collisions in iceberg drift. Such observation are supported by the modeling study described in section 3.

The icebergs we studied drifted west or northwest in all cases, along the front of the parent ice shelf. Some icebergs (e.g., B15a, A38a and b, A39) remained near the ice front, and were seen actually touching the ice front at various times (e.g., Figures 4 and 7). Other icebergs were ejected from the near-ice-front environment relatively early

in their drift (e.g., B16 and B17). For icebergs that drifted out of range for ice-front contact there are sometimes iceberg-on-iceberg collisions. This often happened between the two halves of A38 and B15, and sometimes appeared to cause the two pieces to "jackknife", much as a tractor-trailer behaves in a highway collision. Icebergs B15a and B15b appear to jackknife between the May and August imagery (insets b and c of Figure 4). In the June imagery, B15b is close to the ice front and the western end of B15a is relatively far from the ice front. In the August imagery (inset c of Figure 4), B15b has apparently overtaken B15a and caused B15a to rotate counterclockwise by about 60 degrees, putting the western end of B15a into contact with the ice front. The same process apparently caused a large sliver to break off the northern side of B15a (the sliver is called B15d), and caused B15b to translate northward to a much greater distance from the ice front than it was before the collision.

Icebergs such as A38 and B15 that originate on the eastern side of their parent ice shelf typically take 6 to 8 months to accomplish their westward traverse of the ice front. After reaching the intersection of the ice front and the Antarctic Peninsula (at the Lassiter Coast), pieces of A38 continued to drift along the coast following its northwestern trend. At the time of writing, pieces of B15 had not yet reached the intersection of the ice front and coast near McMurdo Sound, so it remains to be seen whether these iceberg pieces will follow the example of A38 and continue to drift northward along the Victoria Land coast.

While the SSM/I and scatterometer imagery was not sufficiently frequent to resolve tidal motion, the back-and-forth displacements of the icebergs in the analysis of daily

SSM/I and scatterometer imagery suggested the influence of tides (see animations at http://polar.jpl.nasa.gov). Another, indirect indication of the influence of tides on the icebergs is the presence of sea-ice leads which occasionally appear on one side of an iceberg. These long and narrow leads of open water, particularly those occurring during winter, suggest rapid short-term displacements of $O(10)$ km, these being consistent with predicted tidal motions.

3. Numerical Tidal Drift Experiment

We seek to establish the influence of ocean tides on the drift trajectories, post-calving collisions, and break-up of icebergs described in section 2. Following methods established in other studies of iceberg drift, our analysis is based on numerical simulations of iceberg drift in response to the ocean currents and sea-surface tilts. For our tide-only simulations, forcing is provided by a barotropic ocean tidal model.

The numerical experiments we describe integrate linear and angular momentum balance equations through time so as to describe iceberg drift while the icebergs are near the ice front, coast, or each other. Our model experiments differ from previous studies [e.g., *Matsumoto*, 1998; *Gladstone et al.*, in press; *Lichey and Hellmer*, in press] in three ways. First, we consider tidal forcing in isolation from all other oceanic and atmospheric factors that contribute to iceberg drift. We ignore mean, or slowly varying ocean currents, wind stress, and interaction with sea ice, even though we appreciate the role of these processes in real iceberg drift. Second, we explicitly model the drift of a collection of mutually interacting icebergs, each of finite size. Previous studies that

have focused on developing a general climatology for iceberg drift considered icebergs as point entities that do not interact with each other. Third, we allow icebergs to collide as rigid bodies with with ice shelves, coasts and each other. Forces of constraint introduced by the collisions and the rigid body assumption are solved for as unknowns of the linear and angular momentum balance equations. Regardless of whether the primary external forces are tidal or non-tidal, the modeling of finite-sized icebergs with realistic collision dynamics will introduce significant differences to predicted drifts while icebergs are near their parent ice front. If the iceberg manages to escape away from the ice front or coast, the fundamental process to consider (at least in winter) may be the role of sea-ice interactions with icebergs [*Lichey and Hellmer*, in press].

3.1. Tidal Forcing

Tidal forcing for the iceberg-drift integration was obtained from the Circum-Antarctic Tidal Simulation (CATS) model that we have used in other recent studies [*Padman and Kottmeier*, 2000; *Rignot et al.*, 2000]. The CATS model is frequently updated: the version used in the present study is denoted CATS00.1. While updates of the tidal model represent important improvements in the fidelity of the simulated fields to observed counterparts, the initial, exploratory nature of this study does not warrant detailed discussion of the merits of CATS00.1 over its predecessors. The reader is referred to the previously cited studies for further information about CATS: the depth-integrated, shallow water equations on which this model is based are described in *Robertson et al.* [1998], and an example of its performance in the near-ice front

environment is provided by *Rignot et al.*, [2000]. The CATS model was run with a finite-difference grid with ∼5-10 km grid spacing.

The time-varying sea surface elevation, η, and depth-averaged tidal current components, u and v, are evaluated at all vertices of the finite-element mesh defining the present location of the iceberg. This specification uses the usual formulae describing tide height and currents in a flow with multiple tidal constituents:

$$\eta(t,\lambda,\phi) = \sum_{k=1}^{K} \mathcal{Z}_k(\lambda,\phi)\cos(\omega_k t + \zeta_k(\lambda,\phi)) \tag{1}$$

$$u(t,\lambda,\phi) = \sum_{k=1}^{K} \mathcal{U}_k(\lambda,\phi)\cos(\omega_k t + \mu_k(\lambda,\phi)) \tag{2}$$

$$v(t,\lambda,\phi) = \sum_{k=1}^{K} \mathcal{V}_k(\lambda,\phi)\cos(\omega_k t + \nu_k(\lambda,\phi)) \tag{3}$$

In these equations, t is time, λ is longitude, ϕ is latitude, and k denotes the index specifying the tidal constituent (i.e., M_2, S_2, K_2, N_2, $2N_2$, O_1, K_1, and Q_1), $K = 8$ is the total number of tidal constituents considered in this study. The functions $\mathcal{Z}_k$, $\mathcal{U}_k$, and $\mathcal{V}_k$ are the real-valued, spatially variable amplitudes of the sea-surface variation and current components, respectively, and ζ_k, μ_k and ν_k are the real-valued, spatially variable phases of the sea-surface variation and currents, respectively. The ω_k are the frequencies of celestial tidal forcing (periods are listed in Table 1 of *Rignot et al.* [2000]).

We evaluate tide predictions without regard to the locations of the large icebergs. Indeed, the CATS model is based on the ice shelf geometry prior to any of the large calving events reported herein. Our experience suggests that the perturbations of water column thickness associated with a mobile iceberg can have a spatially limited, but

non-negligible influence on tidal amplitude and phase. To see this, note that tidal currents are significantly larger under the leading edge of an ice front than in the open water just north of the front, because the front represents a very short length-scale, large fractional change in water depth. After a calving event, the predicted current for the area previously occupied by shelf ice is, therefore, larger than it would be if the tide model were run again with the revised ice shelf geometry. At the same time, we expect that the currents under the mobile iceberg are actually larger than the model predicts, even when the iceberg is well away from the front. We believe that the simplification of using the pre-calving ice shelf geometry is adequate for the purposes of our study, i.e., for establishing the general patterns of iceberg/tide interaction. Further studies should, however, allow the iceberg drift to feed back into the ocean tidal current predictions. Ideally, this would be done is a truly coupled model, however a more computationally efficient approximation would be to simply scale tidal current predictions to the modified water column thickness in the presence of an iceberg.

3.2. Iceberg Drift Model

The most difficult aspects of our study involve the development of algorithms that detect collisions and the imposition of the constraints of rigid-body motion. In this section we highlight the techniques used to overcome these difficulties. Before discussing these aspects, however, we briefly review the basic dynamical equations for iceberg behavior as used in previous modeling efforts.

3.2.1. Icebergs as Point Entities. Previous studies of iceberg drift have been concerned mainly with long term iceberg-drift climatology, and have thus not considered the influence of iceberg/ice-shelf and iceberg/iceberg collisions that often occur in the days to weeks following calving [*Bigg et al.,* 1997; *Matsumoto*, 1998; *Gladstone et al.,* in press; *Lichey and Hellmer*, in press]. In these cited studies, icebergs are treated as idealized point entities (of zero area and lacking internal angular momentum) governed by a 2-dimensional momentum balance equation:

$$\frac{d\vec{P}}{dt} = -Mf\vec{n}_z \times \vec{U} + \vec{F}_a + \vec{F}_w + \vec{F}_t + \vec{F}_i \tag{4}$$

where $\vec{P}_i$ is the iceberg's linear momentum vector, t is time, M is the mass of the iceberg, $f = 2\Omega\sin(\phi)$ is the Coriolis parameter (Ω is the angular velocity of Earth rotation and ϕ is the latitude), $\vec{n}_z$ is a unit vector pointing vertically, $\vec{U}$ is the horizontal velocity of the iceberg's center of mass, and $\vec{F}_a$, $\vec{F}_w$, $\vec{F}_t$ and $\vec{F}_i$ are the following forces: frictional force of wind; frictional force of ocean current; gravitational force associated with the sea-surface tilt; and force due to interaction with sea ice. The momentum $\vec{P}$ is related to the horizontal coordinates, X and Y, of the iceberg's center of mass by the following relations:

$$\vec{P} \cdot \vec{n}_x = M\dot{X} \tag{5}$$

and

$$\vec{P} \cdot \vec{n}_y = M\dot{Y} \tag{6}$$

where $\dot{X}$ and $\dot{Y}$ are the x- and y-components of $\vec{U}$, $\vec{n}_x$ and $\vec{n}_y$ represent unit vectors in the x- and y- directions, and x and y denote horizontal coordinates on the polar

stereographic projection of the Earth.

3.2.2. Icebergs with Finite Area. Our model of iceberg drift differs from previous models, as described by (4), in 5 important ways. (1) We do not treat icebergs as point objects. We thus compute all forces and accelerations as area integrals over the area of the iceberg. The integral approach we take is especially important for giant icebergs such as B15, where sea-surface slope and tidal currents vary significantly from one end of the iceberg to the other. (2) We compute the angular momentum balance associated with the iceberg's rotation about its center of mass. (3) We introduce a new, heretofore disregarded class of forces: the forces of constraint introduced when an iceberg is in contact with another entity such as an ice front, another iceberg or a coast. To simplify the treatment of collisions, we assume that all collisions are anelastic, i.e., that there is no rebound, and that all icebergs are perfectly rigid. (4) We focus entirely on the influence of ocean tide on iceberg drift. We thus disregard atmospheric effects (i.e., $\vec{F}_a = 0$), sea-ice effects (i.e., $\vec{F}_i = 0$), and non-tidal oceanic effects (done by simplifying $\vec{F}_w$ and $\vec{F}_t$). (5) We consider the interaction between one iceberg and another; i.e., we simulate the drift of more than one iceberg simultaneously in a given model run.

As a result of the 5 differences noted above, the governing equations for linear and relative angular momentum, $\vec{P}_i$ and L_i, respectively, are written:

$$\frac{d\vec{P}_i}{dt} = -\int \alpha f(\vec{k} \times \vec{U}_i) da + (\vec{F}_w)_i + (\vec{F}_t)_i + \vec{C}_{ij} \tag{7}$$

and

$$\frac{dL_i}{dt} = (\mathcal{F}_w)_i + (\mathcal{F}_t)_i + \mathcal{C}_{ij} \tag{8}$$

where,

$$\vec{P}_i \cdot \vec{n}_x = M_i \dot{X}_i \tag{9}$$

$$\vec{P}_i \cdot \vec{n}_y = M_i \dot{Y}_i \tag{10}$$

and

$$L_i = \mathcal{I}_i \dot{\Theta}_i \tag{11}$$

In this set of equations, the following definitions apply: for the i'th iceberg, $f = 2\Omega \sin \phi_i = -1.417 \times 10^{-4}$ s^{-1} is the Coriolis parameter, which we take to be constant; $\alpha = 1.82 \times 10^5$ kg m^{-2} is the mass per unit area, which we take to be constant (computed from the assumptions that a typical iceberg thickness is uniform at 200 m and that the average ice density is 910 kg m^{-3}); $(\vec{F}_w)_i$ is the frictional force of water; $(\vec{F}_t)_i$ is the gravitational force due to sea-surface tilt; $\vec{C}_{ij}$ is the force of constraint due to contact between the i'th and j'th icebergs (the j'th entity can also be an ice front or a coast associated with land); and $(\mathcal{F}_w)_i$, $(\mathcal{F}_t)_i$, and $\mathcal{C}_{ij}$ are the torques about the center of mass associated with forces $(\vec{F}_w)_i$, $(\vec{F}_t)_i$ and $\vec{C}_{ij}$, respectively. The variables Θ_i, $\dot{\Theta}_i$ and $\mathcal{I}_i$ represent the angular orientation, the angular velocity and the moment

of inertia, respectively, of the i'th iceberg with respect to rotation about a vertical axis extending through the iceberg's center of mass. The expression for $\mathcal{I}_i$ is,

$$\mathcal{I}_i = \int \left((x - X_i)^2 + (y - Y_i)^2 \right) \alpha da \tag{12}$$

The integral in (7) is an area integral over the horizontal area of the i'th iceberg, and da is the differential element of area. For simplicity, we disregard variations in iceberg thickness (thus α is uniform) and use an $f-$plane approximation (constant Coriolis parameter). In this circumstance, the Coriolis acceleration does not appear as a torque in (8) and L_i may be associated with that part of the angular momentum that is associated with motion (i.e., the angular momentum associated with the f-plane rotation does not change).

In our model, momentum balance in the third, vertical dimension is assumed to express a condition of neutral flotation, i.e., the iceberg is everywhere in local hydrostatic equilibrium. The iceberg is thus assumed to be an elastic plate with zero flexural rigidity, i.e., the elastic restoring forces that occur when the iceberg flexes to conform to the shape of the ocean surface is negligible. In other words, the iceberg is able to drape freely across the perturbed ocean surface without perturbing the pressure field in the water column below. This assumption is justified by the fact that the length scale over which flexural rigidity effects come in to play ($\sim$1 km, related to ice thickness) is 2 orders of magnitude less than the length scale over which the tide typically deforms the sea surface (i.e., $\sim$100 km) [*Padman and Kottmeier*, 2000]. This assumption of zero flexural rigidity is restricted to consideration of how an iceberg deforms to fit the ocean

surface that has been disturbed by tides. Where we consider collisions and subsequent potential deformations in the horizontal plane, we assume that the iceberg is perfectly rigid.

To account for variation of ocean tide variables over the finite extent of the iceberg's area, we perform area integrations, using a standard finite-element algorithm, to compute forces and torques. The expressions for $\vec{F}_w$ and $\vec{F}_t$ are

$$\vec{F}_w = -\int \rho_w k \left((\dot{x} - u)\, \vec{n}_x + (\dot{y} - v)\, \vec{n}_y \right) \sqrt{(\dot{x} - u)^2 + (\dot{y} - v)^2} da \tag{13}$$

$$\vec{F}_t = -\int (\alpha g \nabla \eta)\, da \tag{14}$$

In these equations, the domain of integration is the iceberg area, $g = 9.81$ m s^{-2} is the acceleration of gravity, $\nabla\eta$ denotes the gradient of the sea surface elevation, $\rho_w = 1028$ kg m^{-3} is the density of seawater in which the iceberg floats, and $k = 0.002$ is a coefficient of friction (assuming a quadratic friction law for differential iceberg/seawater motion). Variables $\dot{x}$ and $\dot{y}$ denote the local horizontal velocity of points on the iceberg, and are computed using the rigid-body assumption,

$$\dot{x} = \dot{X} - \dot{\Theta}(y - Y) \tag{15}$$

and

$$\dot{y} = \dot{Y} + \dot{\Theta}(x - X) \tag{16}$$

where $\dot{\Theta}$ is the angular velocity of rotation about a vertical axis through the center of area. Variables $(\dot{x} - u)$ and $(\dot{y} - v)$ denote the relative velocity of the iceberg and the water below the iceberg.

The expressions for $\mathcal{F}_w$ and $\mathcal{F}_t$ are generated through the use of cross products,

$$\mathcal{F}_w = \int \vec{r} \times \vec{F}_w da \tag{17}$$

$$\mathcal{F}_t = \int \vec{r} \times \vec{F}_t da \tag{18}$$

where $\vec{r} = (x - X)\vec{n}_x + (y - Y)\vec{n}_y$.

3.2.3. Free Drift vs. Constrained Drift. The most important aspect of the model to distinguish it from previous treatments of iceberg drift is the existence of two modes of iceberg drift, free drift and constrained drift. When the icebergs are not touching, $\vec{C}_{ij} = 0$ and $\mathcal{C}_{ij} = 0$. In this circumstance, (7) and (8) represent $3N$ equations which can be solved for $3N$ unknowns: $\dot{X}_i$, $\dot{Y}_i$, and $\dot{\Theta}_i$, for $i = 1, \ldots, N$. This allows X_i, Y_i and Θ_i to be updated by simply summing the forces and torques acting on each individual iceberg in isolation.

When icebergs are in contact with other icebergs, the ice shelf or coasts, the solution to (7) and (8) becomes more complicated. Forces of constraint and related torques, $\vec{C}_{ij}$, and the $\mathcal{C}_{ij}$, are unknowns. Furthermore, situations arise where there are more unknowns than equations of constraint, i.e., the equation set is rank-deficient. Consider, for example, a collection of N icebergs in which there are K points of contact between various icebergs and their surroundings. In this situation, the forces and torques of constraint introduce $6K$ new unknowns to the problem of balancing forces and torques. To see how K points of contact multiply into $6K$ additional unknowns, consider the forces of constraint and torques involved in one single contact between two icebergs. For the k'th contact, which we assume to be between icebergs labeled p and q, 4 unknowns

are represented by the x- and y- components of $\vec{C}_{pq}$ and $\vec{C}_{qp}$. Two more unknowns are represented by the two torques $\mathcal{C}_{pq}$ and $\mathcal{C}_{qp}$. Along with the $3N$ unknowns that are also active during free drift, i.e., $\dot{X}_i$, $\dot{Y}_i$, and $\dot{\Theta}_i$, for $i = 1, \ldots, N$, the total number of unknowns in a system with K points of contact becomes $3N + 6K$, which is greater than the $3N$ equations represented by (7) and (8).

We must, therefore augment the equations for linear and angular momentum with additional physical constraints so that a unique solution describing the motion of the collection of icebergs can be determined. We appeal to the rigid-body assumption and the definition of torque to accomplish this. The rigid-body assumption, i.e., that the plan-view shape of the icebergs and other entities (coasts and ice shelves) is fixed and independent of the strength of collisional forces, provides 2 constraints for every point of iceberg/iceberg or iceberg/ice-shelf contact. To see this, consider the k'th contact that involves icebergs labeled p and q. The rigid body assumption requires that each iceberg does not deform the shape of the other; thus the two points on the perimeters of each iceberg that define the point of contact must move with the same velocity. (The situation when the two icebergs move apart from an initial state of contact is discussed later.) Describing each point's motion as the sum of a center of area motion and a rotational motion, the two equations of constraint are represented by the following vector equation,

$$\dot{\vec{U}}_p + \dot{\Theta}_p \times \vec{r}_p = \dot{\vec{U}}_q + \dot{\Theta}_q \times \vec{r}_q \tag{19}$$

where vectors $\vec{r}_p$ and $\vec{r}_q$ define the position of the points of contact relative to the center

of area of each of the two icebergs. Figure 8 provides a schematic view of the geometry of two icebergs in contact. Figure 8

Forces exchanged between colliding bodies are equal and opposite. We may thus write 2 additional equations for the k'th contact between icebergs p and q. Again, this is a vector equation:

$$\vec{C}_{pq} = -\vec{C}_{qp} \tag{20}$$

Finally, the definition of torque also yields 2 equations for the k'th contact between icebergs p and q:

$$\mathcal{C}_{pq} = \vec{r}_p \times \vec{C}_{pq} \tag{21}$$

and

$$\mathcal{C}_{qp} = \vec{r}_q \times \vec{C}_{qp} \tag{22}$$

Along with the $3N$ equations describing conservation of linear and angular momentum, the above $6K$ equations of constraint can, in principle, be solved for the $3N + 6K$ unknowns that completely describe the iceberg's motion and all forces and torques generated through their rigid contact.

The second complication of constrained drift arises because the $6K$ independent constraints described above are not always independent. This leads to a rank-deficient set of equations, mandating careful consideration of the non-uniqueness of the resulting solutions. To illustrate this, we describe a typical example of how it arises. Consider the collisional geometry displayed in Figure 9. In this geometry, a single iceberg has become wedged within a V-shaped embayment in the front of a rigid ice shelf. The two Figure 9

points on the iceberg's perimeter in contact with the ice shelf are labeled A and B. The immobility of the ice shelf forces us to realize that the iceberg cannot move without forcing either point A or point B to penetrate the ice shelf. We deduce that $\dot{X}$, $\dot{Y}$ and $\dot{\Theta}$ of the iceberg are zero. Making use of (20), (21) and 22), the number of unknowns in this system is now reduced to 4, namely the two components of force transmitted across the iceberg/ice shelf contacts at points A and B: $(\vec{C}_A)_x$, $(\vec{C}_A)_y$, $(\vec{C}_B)_x$ and $(\vec{C}_B)_y$. Having exhausted all of the constraint equations of the type (19), (20), (21) and 22), we are left with only 3 equations stemming from (7) and (8) to determine 4 unknowns. This is a rank-deficient system; the number of unknowns exceeds the number of constraints.

The physical reasoning behind the rank-deficiency illustrated by the above example is that an arbitrary force of constraint generated at point A, say $(\vec{C}_A)_x$, can be exactly cancelled by a constraint force generated at point B, i.e., $(\vec{C}_A)_x = -(\vec{C}_A)_x$. In this circumstance, there are an infinite number of equally valid solutions of (7) and (8) which differ only by the magnitude of the cancelling forces generated at A and B.

To cope with rank deficiency we use singular-value decomposition (SVD). One property of SVD is that whenever there are an infinite number of solutions differing only by an arbitrary constraint force, the solution in which that arbitrary force is zero is chosen. In the example above, the SVD selects a solution where $(\vec{C}_A)_x = 0$.

3.2.4. Collision Kinematics and Dynamics. Much of the numerical implementation of our scheme for the drift of a collection of finite-dimension icebergs is straightforward. Two aspects of the numerical techniques, however, were of sufficient difficulty to merit discussion here. The first is the problem of determining when

an iceberg collides with another iceberg, ice shelf or coast. The second involves the determination of when an iceberg and ice shelf, or two icebergs, drift apart after some period of contact.

To perform these determinations, we treat the boundaries of icebergs, ice fronts and coasts as composed of vertices connected by line segments. A collision is typically characterized by the vertex of one iceberg coming into contact with a line segment belonging to another. An example of a collisional geometry is shown in Figure 10. At the end of each time step, the model scans all vertices to determine if the trajectory of any have crossed line segments at any time during the time step. In other words, we determine if any vertex of one iceberg has entered the region occupied by another iceberg or ice shelf. This determination is made using the MatLab computer programming language using an algorithm that determines if an arbitrary point is inside the region bounded by a polygon. (If the point is inside the polygon, the sum of angular displacements of a vector between the point in question and each successive point on the perimeter of the polygon is 2π.)

Figure 10

When one or more such vertices are identified, the time step is retaken in several substeps. The first substep is the portion covering the time span before the particular vertex that crossed a line segment earliest comes into contact with the line segment. The subsequent substeps, which can be one if no other vertices cross line segments, cover the remaining span of the original time step, but do so with the additional constraints imposed by the vertex/line-segment contact achieved during the first substep.

To determine the exact moment during a time step when a vertex defining the

perimeter of one iceberg crosses a line segment defining the boundary of another, we use an algorithm that involves cross products between various vectors defined by the initial and final positions of the vertex in question and the end points of the line segment in question. An example of how this algorithm is used to determine the exact position of vertices and line segments defining the perimeters of icebergs at the moment of collision is shown in Figure 10.

The algorithm used to identify collisions is not perfect, but it has two virtues: it is relatively efficient computationally, and it never reports a collision when none in fact has occurred. It is, however, possible for the algorithm to fail to report a collision, such as when a vertex of one iceberg sweeps completely through a corner of another iceberg in a single time step. We believe that simulations described below were not significantly influenced by this possibility.

As the physical basis for deciding when to disengage an iceberg from an ice shelf, or two icebergs from each other, we assume that forces of constraint, i.e., $\vec{C}_{ij}$, cannot be tensile across iceberg boundaries. This assumption is common in the treatment of collisions of cohesionless rigid bodies. To test for tensile forces of constraint, $\vec{C}_{pq} \cdot \vec{n}$ is evaluated at the end of each time step: if $\vec{C}_{pq} \cdot \vec{n} > 0$, the force of constraint is tensile across the line segment on which the vertex is in contact. (In this test, $\vec{n}$ is the appropriate outward pointing normal vector.) When tensile stress is detected, the time step is retaken without imposing any of the constraints of contact formerly associated with $\vec{C}_{pq}$, i.e., the vertex is free to move away from the line segment.

4. Iceberg Drift Experiments

Three sets of simulations were conducted to investigate the tide-driven drift of icebergs: (1) the 1998 calving event in the Weddell Sea (A38 and A39); (2) the early 2000 calving event in the Ross Sea (B15 - B18); and (3) the mid-2000 calving event in the Weddell Sea (A43 and A44). Because tidal currents are much stronger in the Weddell Sea than in the Ross Sea (compare *Robertson et al.* [1998] with (*MacAyeal* [1984), the simulation in the Ross Sea was run for 365 days to generate roughly the same net iceberg drift as the 50 and 60 day runs that were used to simulate the Weddell Sea icebergs. In all cases, simulations were begun with initial conditions representing an iceberg at rest in its initial, post-calving position, i.e., nestled into the ice-shelf embayment from which it calved. The tidal forcing was synchronized with the times that the icebergs were first discovered, believed to be within a day of actual calving. Some simulations were repeated to investigate the effects of iceberg break-up following calving. In one case, the icebergs were left intact. In other cases, the icebergs were initially specified as being in their broken condition. The model does not simulate the actual break-up of an iceberg. This interesting problem is left for future research.

4.1. Drift of A38 and A39

Several different simulations were conducted to investigate the drift of various pieces of A38 and A39. The results are summarized in Figures 11 and 12. Each run simulated a 60-day period beginning on October 13, 1998 at 00:00 GMT. The exact time of A38's detachment from the Ronne Ice Shelf is unknown, however satellite imagery described

Figures 11 a

previously suggests that the iceberg calved on this date. The simulated trajectory which compares most favorably with the satellite observations (section 2) was obtained when the model was initiated with A38 in its broken condition (i.e., the pieces of A38 are initially distinct, albeit positioned so as to assemble the iceberg as a single entity). In this favorable simulation (Figure 11), A38b, A39 and various other pieces traverse the length of the ice front and subsequently turn the corner where the ice front meets the Antarctic Peninsula. While model drift agrees qualitatively with the actual drift of A38a, A38b and A39, modeled net drift along the ice front and coast is too rapid. This difference may be due to additional friction imposed by interaction with sea ice, as discussed by *Lichey and Hellmer* [in press], which is not accounted for in this study. Alternatively, the result may be caused by the use of pre-calving ice shelf geometry for the ocean tidal model (see discussion is section 3.1). The complex problem of truly coupling the iceberg drift model to the tidal prediction model is left to future studies.

Another difference between the simulation (Figure 11) and the observations is that A38a, the eastern half of A38 after its break-up, is ejected from the near-ice front environment relatively soon after the start of the simulation. The effect of this is profound. Instead of drifting along the ice front with A38b and A39, A38a remains nearly stationary, following a closed elliptical orbit typical of free-drift tidal motion. This effect highlights the role of iceberg-ice shelf collisions as an important factor in rectifying otherwise periodic tidal motions.

The influence of collisions on tide-driven drift is also highlighted by a simulation in which A38 alone, in its unbroken configuration, is allowed to interact with the ice front

through a 60-day period. This simulation, and another in which A38b, alone, is allowed to drift in isolation (Figure 12), show that collisions with the ice front rectify what would otherwise be closed elliptical orbits of the icebergs' trajectories. The trajectories of the center of areas in each simulation form helical paths (Figure 12). Some tidal rectification may occur even without inclusion of collision dynamics. Mean Lagrangian drift of water parcels is a common outcome of tidal flow in regions of rapid variations in water depth [e.g., *Padman et al.* 1992; *Makinson and Nicholls*, 1999]. We examined the Lagrangian mean drift of an individual water parcel that is not constrained by collisions with the ice front, i.e., the water can slide underneath the ice shelf. The initial position of the water parcel was taken to be that of the A38's center of area. These simulation places a limit on how much of the net drift is explicable only by invoking the kedging effect.

Various ways in which an iceberg interacts with the remnant ice front are shown in Figure 13. The iceberg drifts freely with the tide when the tidal current and sea surface slope direct the iceberg to the north and west. When the tidal current and sea surface slope are in an adverse direction (south and east), the iceberg holds fast against the ice front. Once the iceberg is again released from the ice front, it is accelerated by the steep sea-surface slope and tidal current. This further amplifies the difference between the iceberg's motion and that of a water parcel. Notable features of the drift experiment results are the frequency and severity of A38's collisions with the ice front, particularly in the vicinity of the iceberg's region of origin. As shown in panel (a) of Figure 13, which displays a simulation of A38 in its pre-break-up configuration, A38

Figure 13

spends several days battering the ice-front promontory defining the western end of the ice-front embayment created by the iceberg's detachment. The impulse imparted to the ice front associated with such collisions is illustrated in Figure 14.

Figure 14

The battering behavior occurred relatively soon after A38 calved in the simulation, and this leads us to speculate that such tide-driven behavior led to the break-up of A38 into pieces as seen in the SAR amplitude imagery of October 22, 1998, about 9 days after the iceberg originally calved (see Figure 7). The break off of the ice-front promontory forming the western end of the ice-front embayment created by A38's detachment, i.e., the calving of A39, is also likely to have been stimulated by the battering behavior of A38.

4.2. Drift of B15-B18 and A43-A44

The behavioral features of tide-driven iceberg drift associated with simulations of icebergs B15-B18 and A43-A44, calved into the Ross and Weddell seas, respectively, show little difference with those discussed in section 4.1 for A38-A39. As mentioned above, the simulation of B15-B18 (Figure 15) was conducted for a 365-day period to account for the reduced tidal amplitudes in the Ross Sea relative to the Weddell Sea. The simulation of A43-A44 (Figure 16) was conducted for a 50-day period.

Figure 15

Figure 16

Each of these simulations shows good qualitative agreement with the satellite observations described in section 2. In each case, the icebergs drift westward along the ice front. In the case of the Weddell Sea icebergs (A43 and A44), which started closer to the western end of the ice front than other icebergs, drift continued up the coast

after the icebergs turned the corner made by the intersection of the ice front and coast. Presumably analogous northward travel along the coast of the Ross Sea will be the fate of B15-B18 after more than a year of drift.

5. Summary

Numerical simulations were used to investigate the role of time-varying forcing in the initial drift of large tabular icebergs. We consider here only tidal forcing, which is relatively predictable and is believed to provide a major part of the total external forces on an iceberg in the near-ice-front environment. Good qualitative agreement between simulated drift behavior and observations provided by satellite imagery lead us to believe that tides do indeed exert a strong influence on the the immediate post-calving behavior of these icebergs. This influence arises as follows.

Immediately after a major calving event, icebergs can experience frequent collisions with the remnant ice front because of the periodic tides. This may be the principal cause of iceberg break-up and sympathetic calving from parts of the ice shelf into which the iceberg collides. Calving stimulated by iceberg battering thus may represent an important process that smoothes the geometry of what would otherwise evolve as a jagged ice front.

The tidal model predicts the observed westward drift of new icebergs along the remaining ice front. Given that our simulations explicitly exclude all other forms of oceanic and atmospheric forcing, we cannot establish that tides alone, in concert with the collisions they cause, are responsible for this westward drift. There may indeed be

other processes associated with ocean current and wind which lead to the same effect, and this idea has strong support from previous work [e.g., *Gladstone et al.,* in press; *Lichey and Hellmer,* in press]. Nevertheless, the agreement between our simulations and the iceberg trajectories observed with satellite imagery is sufficiently strong to suggest that tidal forcing, at least while the icebergs are able to intermittently make contact with the ice front, is a significant component of mean along-front drift, and should be considered in future efforts to study iceberg drift.

To further examine the immediate post-calving behavior of large, tabular icebergs using observational techniques, the frequency with which iceberg position and shape are observed must resolve the tidal variability, requiring sampling at $O(1)$ h intervals. To this end, GPS tracking devices (along with automatic weather stations) were deployed on B15a on January 25, 2001. These devices are designed to provide positions accurate to 5 m every 30 minutes, and to relay the information via the ARGOS satellite to our institutions for further analysis. An initial use of this data, once a significant time period has accumulated, will be to evaluate the role of tidal kedging in iceberg drift relative to other forms of external forcing.

Improved iceberg drift forecasting may be best addressed by increasing the sophistication of numerical models of iceberg behavior. Here we have demonstrated the need to consider each iceberg as a finite-area entity (i.e., which necessitate treatment by area integration of various external forces in iceberg drift models), whose multiple collisions with ice shelves, coasts, and other icebergs significantly modifies the iceberg's behavior relative to models in which the iceberg is treated as a point entity in free drift.

Within this paper we have identified two areas in which improvements could be made, true or parameterized coupling of the ocean tidal forecast model with the iceberg drift model, and incorporation of ice mechanics and thermodynamics to predict both the initial calving event and subsequent breakup of nascent icebergs. Other studies have considered the possibly critical role of sea ice in modifying an iceberg's drift response to wind, tides, and other ocean currents. A synthesis of these concepts, combined with improved realism of the total oceanic and atmospheric forces that act on any specific iceberg, is the logical next step towards improved forecasting skill.

Acknowledgments. The list of authors' names appearing in the title is in alphabetical order beyond the second author. While all authors contributed in a substantial and essential way to the intellectual content of the research presented here, the particular emphasis of this work (and mistakes which may result from this emphasis), are primarily the responsibility of the first author. Work performed at the Jet Propulsion Laboratory, California Institute of Technology was supported by a contract with the National Aeronautics and Space Administration (NASA). Support for the University of Chicago component of this project was provided by the National Science Foundation Office of Polar Programs (OPP-9818622). The satellite data needed for this research were provided by the European Space Agency (ERS-1/2 project code: AO2.USA.160). The ocean tidal modeling at Oregon State University (OSU) and Earth & Space Research (ESR) was supported by grants from the National Science Foundation Office of Polar Programs (OPP-9615525 and OPP-9896041), and from NASA (NAG5-7790). Gary Egbert and Lana Erofeeva at OSU provided advice and computer resources for running the tidal model. The field project referenced in the summary is supported by the National

Science Foundation Office of Polar Programs (IO-190-0). Numerous colleagues provided supportive guidance and healthy skepticism throughout the conduct of the research presented here. We specifically mention Christina Hulbe and Stan Jacobs.

References

Bigg, G. R., Wadley, M. R., Stevens, D. P. and J. A. Johnson, Modelling the dynamics and thermodynamics of icebergs, *Cold Reg. Sci. and Tech., 26*, 113-135, 1997.

Drinkwater M.R., Satellite Microwave Radar Observations of Antarctic Sea Ice, *In* C. Tsatsoulis and R. Kwok (Eds.), *Analysis of SAR Data of the Polar Oceans*, Chapt. 8, 145-187, Springer-Verlag, Berlin, 1998.

Gladstone, R. M., G. R. Bigg, and K. W. Nicholls, Iceberg trajectory modelling and meltwater injection in the Southern Ocean, *J. Geophys. Res.*, in press.

Holdsworth, G., Tidal interaction with ice shelves, *Ann. Geophys., 33*, 133-146, 1977.

Jacobs, S. S., D. R. MacAyeal, and J. L. Ardai, Jr., The recent advance of the Ross Ice Shelf, Antarctica, *J. Glaciol.*, *32*, 464-474, 1986.

Jacobs, S. S., H. Hellmer, C. Doake, and R. Frolich, Melting of ice shelves and the mass balance of Antarctica, *J. Glaciol.*, *38*, 375-387, 1992.

Keys, H. J. R., S. S. Jacobs, and D. Barnett, The calving and drift of iceberg B9 in the Ross Sea, Antarctica, *Ant. Sci.*, *2*(3), 243-257, 1990.

Lazzara, M. A., K. C. Jezek, T. A. Scambos, C. J. van der Veen , and D. R. MacAyeal, On the recent calving of icebergs from the Ross Ice Shelf, *Polar Geo.*, *23*, 201-212, 1999.

Lichey, C. and H. H. Hellmer, Modeling giant iceberg drift under the influence of sea ice, *J. Glaciol.*, in press.

MacAyeal, D. R., Numerical simulations of the Ross Sea tides, *J. Geophys. Res.*, *89*, 607-615, 1984.

Makinson, K., and K. W. Nicholls, Modeling tidal currents beneath Filchner-Ronne Ice Shelf and on the adjacent continental shelf: their effect on mixing and transport, *J. Geophys.*

Res.,, *104*, 13,449-13,465, 1999.

Matsumoto, K., An iceberg drift and decay model to compute the ice-rafted debris and iceberg meltwater flux: An application to the interglacial North Atlantic, *Paleoceanography*, *11*, 729-742, 1996.

Nøst, O. A., and S. Østerhus, Impact of grounded icebergs on the hydrographic conditions near the Filchner Ice Shelf, in: *Ocean, Ice, and Atmosphere, Interactions at the Antarctic Continental Margin*, *75*, S. S. Jacobs and R. F. Weiss, editors, pp. 267-284, AGU, Washington, D.C., 1998.

Padman, L., and C. Kottmeier, High frequency ice motion and divergence in the Weddell Sea, *J. Geophys. Res.*, it 105, 3379-3400, 2000.

Padman, L., A. J. Plueddemann, R. D. Muench, and R. Pinkel, Diurnal tides near the Yermak Plateau, *J. Geophys. Res.*, *97*, 12,639-12,652, 1992.

Rignot, E., and D. R. MacAyeal, Ice-shelf dynamics near the front of the Filchner-Ronne Ice Shelf, Antarctica, revealed by SAR interferometry, *J.Glaciol.*, *44*, 405-418, 1998.

Rignot, E., L. Padman, D. R. MacAyeal and M. Schmeltz, Observation of ocean tides below the Filchner and Ronne Ice Shelves, Antarctica, using synthetic aperture radar interferometry: Comparison with tide model predictions, *J. Geophys. Res.*, *105*, 19,615-19,630, 2000.

Robertson, R. A., L. Padman, and G. D. Egbert, Tides in the Weddell Sea, in: *Ocean, Ice, and Atmosphere, Interactions at the Antarctic Continental Margin*, *75*, S. S. Jacobs and R. F. Weiss, editors, pp. 341-369, AGU, Washington, D.C., 1998.

Scambos, T.A, C.L. Hulbe, M.A. Fahnestock, and J. Bohlander, The link between climate warming and Break-up of ice shelves in the Antarctic Peninsula, *J. of Glaciol.*, *46*,

516-530, 2000.

Smithson, M. J., A. V. Robinson, and R. A. Flather, Ocean tides under the Filchner-Ronne Ice Shelf, Antarctica, *Ann. Glaciol.*, *23*, 217-225, 1996.

Skvarca, P., W. Rack, H. Rott and T. Ibarzábal y Donángelo, Climatic trend and the retreat and disintegration of ice shelves on the Antarctic Peninsula: an overview, *Polar Res., 18*, 151-157, 1999.

Vaughan, D., and C. Doake, Recent atmospheric warming and retreat of ice shelves on the Antarctic Peninsula, *Nature*, *379*, 328-, 1996.

T. T. Gotis, B. Kerman, and D. R. MacAyeal, Department of Geophysical Sciences, University of Chicago, 5734 S. Ellis Ave., Chicago, IL 60637. (drm7@midway.uchicago.edu)

L. Padman, Earth & Space Research, 1910 Fairview Avenue East, Suite 102, Seattle, WA 98102-3620. (padman@esr.org)

M. Fahnestock, Department of Geophysical Sciences, University of Maryland, College Park, MD 20742. (mark@metosrv2.umd.edu)

M. Drinkwater, ESTEC, European Space Agency, Keplerlaan 1, P. O. Box 299, 2200 AG Noordwijk ZH, The Netherlands. (mkrinkwa@estec.esa.nl)

T. Scambos, National Snow and Ice Data Center, CIRES Campus Box 449, University of Colorado, 1540 30th St., Boulder, CO 80309. (teds@icehouse.colorado.edu)

E. Rignot, Jet Propulsion Laboratory, California Institute of Technology, MS 300-235, 4800 Oak Grove Drive, Pasadena, CA 91109. (eric@adelie.jpl.nasa.gov)

A. L. Gray, CCRS, 588 Booth Street, Ottawa, Ontario, Canada, K1A 0Y7.

(Laurence.Gray@CCRS.NRCan.gc.ca)

M. Lazzara and C. Stearns, Antarctic Meteorological Research Center, Space Science and Engineering Center, University of Wisconsin, 1225 West Dayton Street, Madison, WI 53706. (mattl@ssec.wisc.edu)

Received _____

[1]Department of Geophysical Sciences, University of Chicago, Chicago, Illinois.

[2]Earth and Space Research, Seattle, Washington.

[3]ESTEC, European Space Agency, Noordwijk, The Netherlands.

[4]Department of Geophysical Sciences, University of Maryland, College Park, Maryland.

[5]CCRS, Ottawa, Ontario, Canada.

[6]Antarctic Meteorological Research Center, Space Science and Engineering Center, University of Wisconsin, Madison, Wisconsin.

[7]Jet Propulsion Laboratory, California Institute of Technology, Pasadena.

[8]National Snow and Ice Data Center, University of Colorado, Boulder.

Manuscript for submission to the *Journal of Geophysical Research*, March 2001.

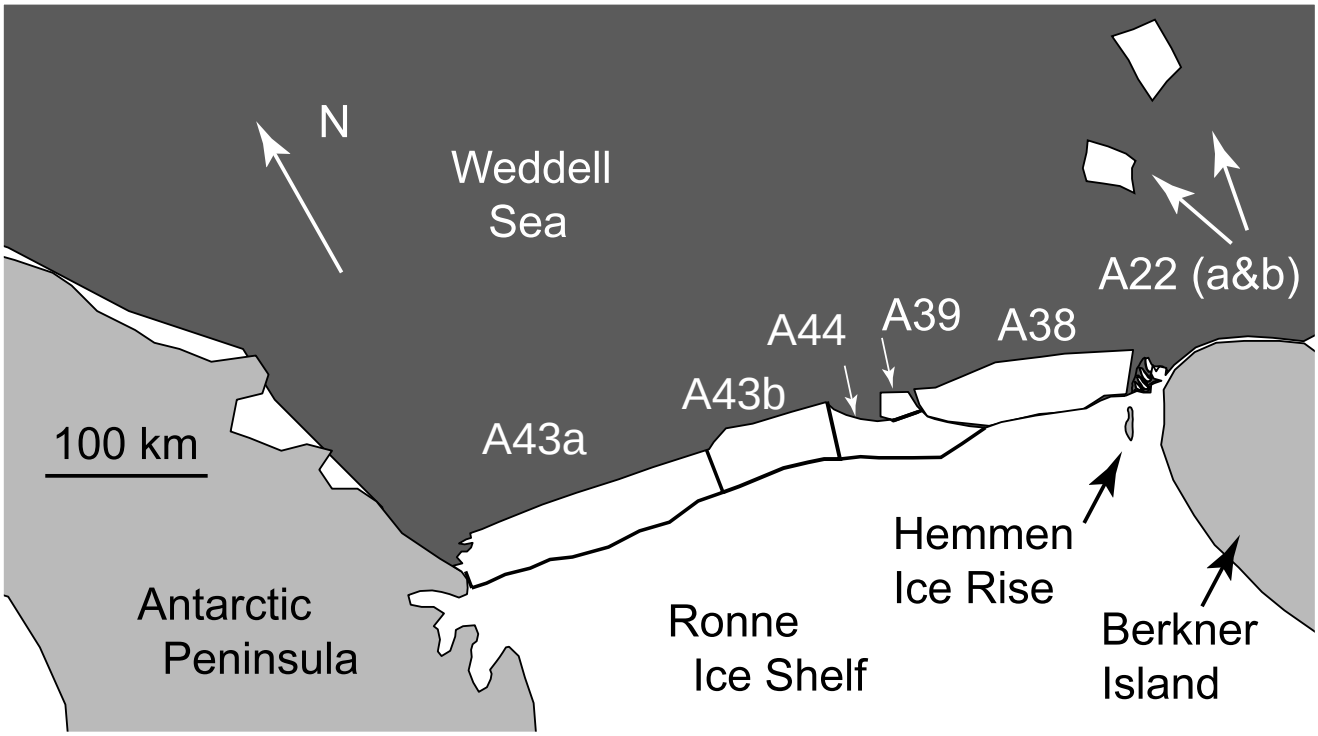

Figure 1. Start positions of A38 and A39, which calved in October, 1998, and start positions of A43a, A43b and A44, which calved in May, 2000 (polar stereographic projection). Light gray represents grounded ice. or . Black represents open water, including regions of seasonal or perennial sea ice. White represents floating ice shelf and icebergs, including A22a and A22b that are presently grounded on the Berkner Bank (see *Nøst and Østerhus* [1998] for the history of A22).

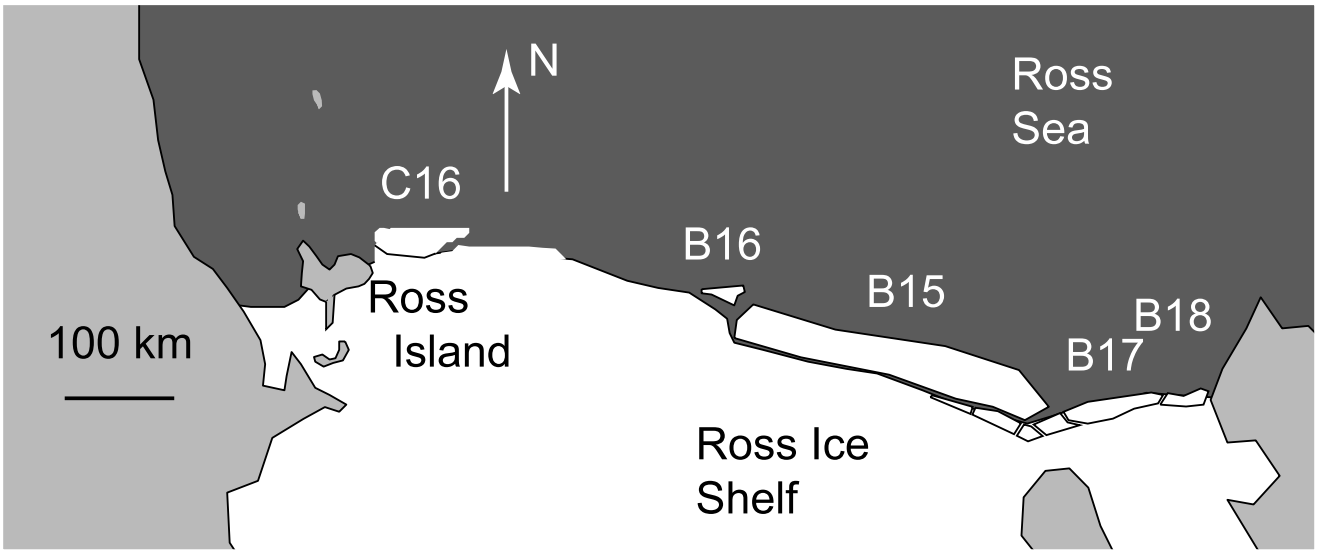

Figure 2. Start positions of B15 through B18 and C16, which calved between March and May, 2000 (polar stereographic projection). Light gray represents ice free land or grounded ice. Black represents open water, including regions of seasonal or perennial sea ice. White represents the floating ice shelf and icebergs.

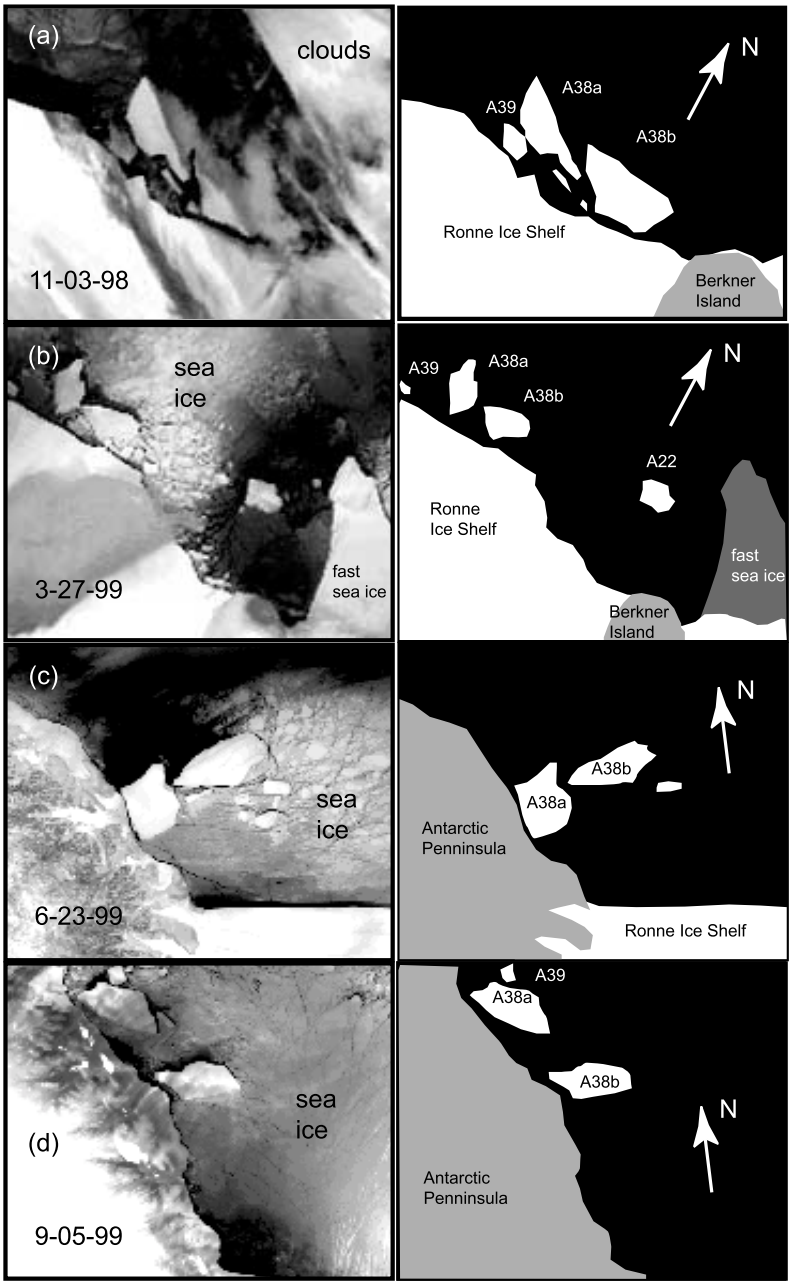

Figure 3. Advanced very-high resolution radiometer (AVHRR) imagery of icebergs A38 and A39 over a 10-month period following calving. (Actual dates, panels (a) to (d): November 3, 1998; March 27, 1999; June 23, 1999; and September 5, 1999.) Sketch maps on right are provided to help distinguish icebergs, grounded ice and ice shelf from cloud cover and sea ice. Map scale is variable. For reference, A38b is approximately 50 km long by 30 km wide.

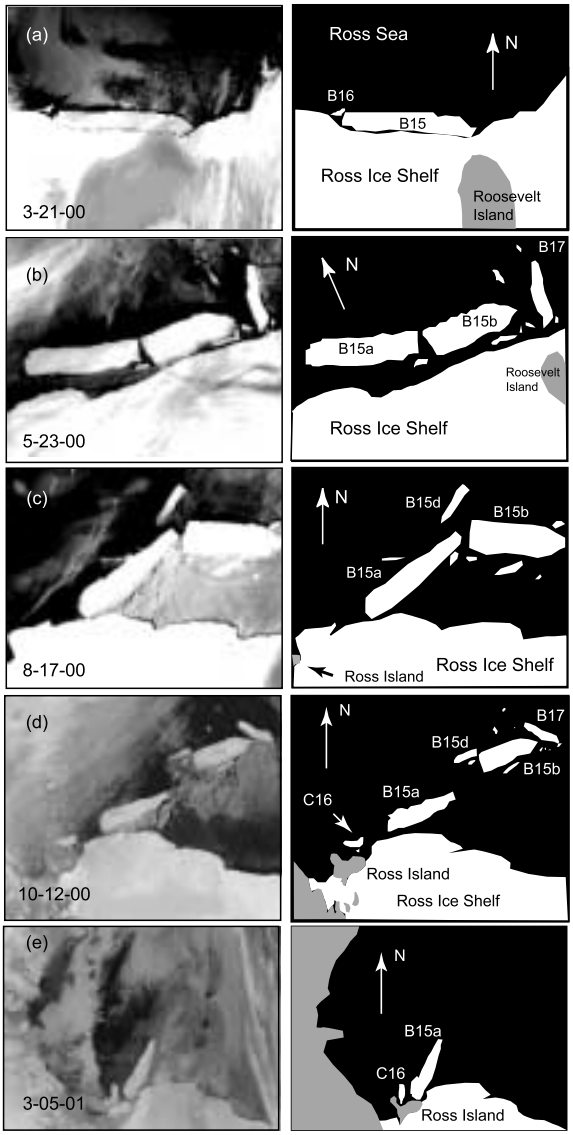

Figure 4. Advanced very-high resolution radiometer (AVHRR) imagery of icebergs B15 through B18, and C16 over a 12-month period following calving. (Actual dates, panels (a) to (e): March 21, 2000; May 23, 2000; August 17, 2000; October 12, 2000; and March 5, 2001.) Sketch maps on right identify features in the imagery. Map scale is variable across panels (a) to (e). For reference, B15a is approximately 150 km long and 40 km wide.

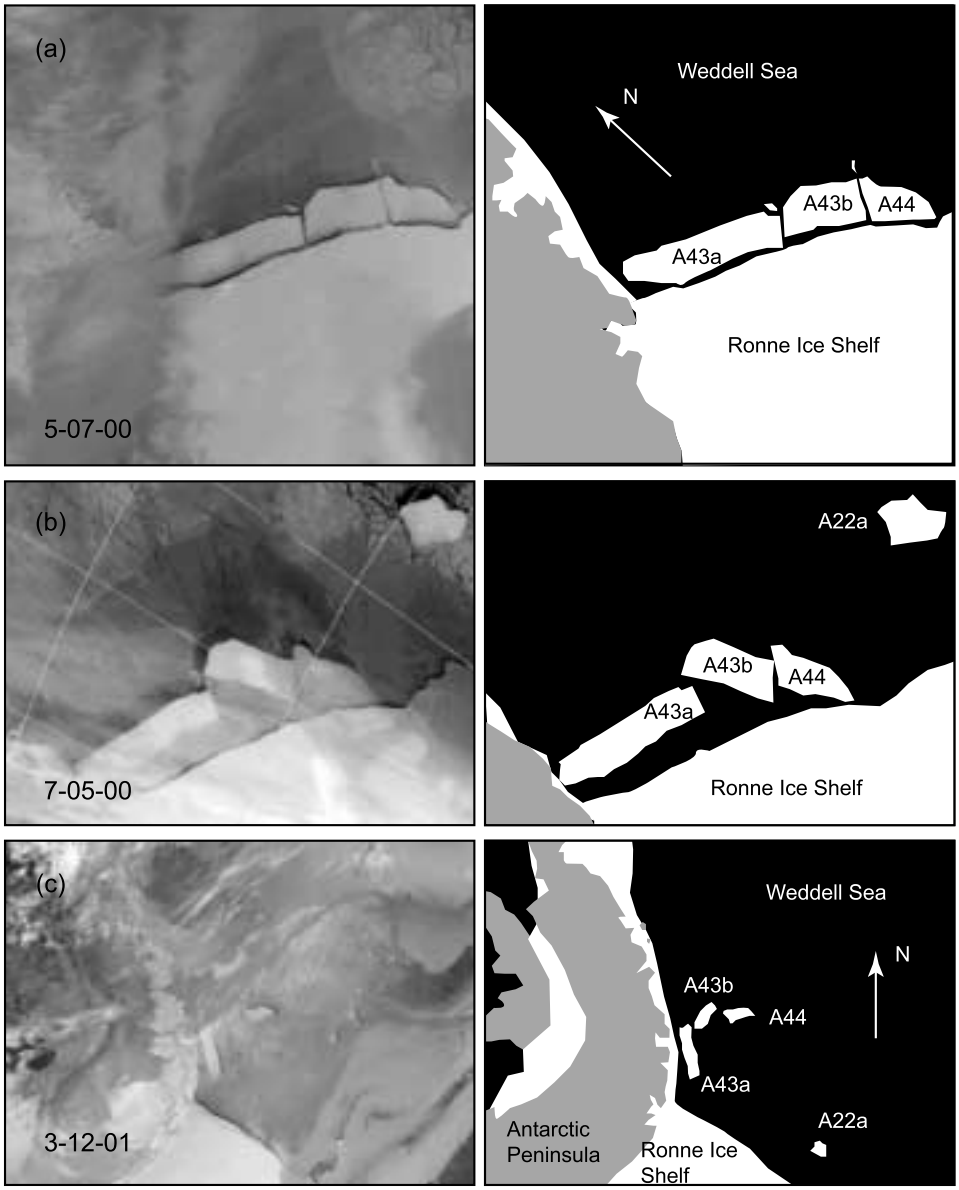

Figure 5. Advanced very-high resolution radiometer (AVHRR) imagery of icebergs A43 and A44 over a 9-month period following calving. (Actual dates, panels (a) to (c): May 7, 2000; July 5, 2000; and March 12, 2001.) Sketch maps on right identify features in the imagery. Map scale is variable. For reference, A43a is approximately 175 km long and 40 km wide.

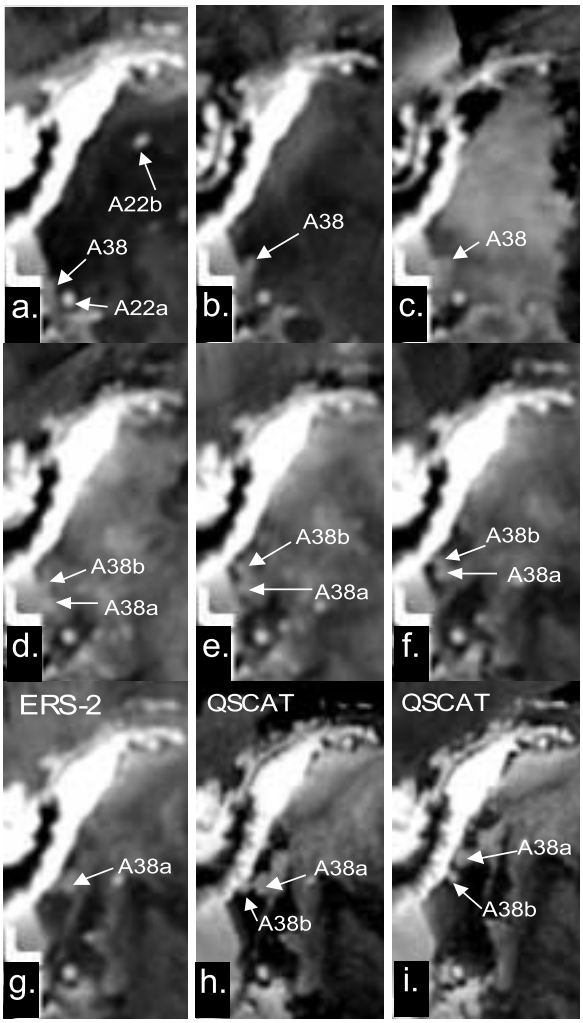

Figure 6. Microwave radar scatterometer images of the southwest Weddell Sea, Ronne Ice Shelf and Antarctic Peninsula covering a 1-year period from October, 1998 to July, 1999. Panels (a)-(g) show ERS-2 C-band radar images for days (a) October 21, 1998; (b) December 11, 1998; (c) January 22, 1999; (d) March 25, 1999; (e) April 21, 1999; (f) June 2, 1999; (g) July 20, 1999. Images (h) and (i) are QSCAT Ku-band radar images for days (h) July 20, 1999 and (i) September 3, 1999. The locations of one or more pieces of iceberg A38 are indicated where clearly visible in the imagery.

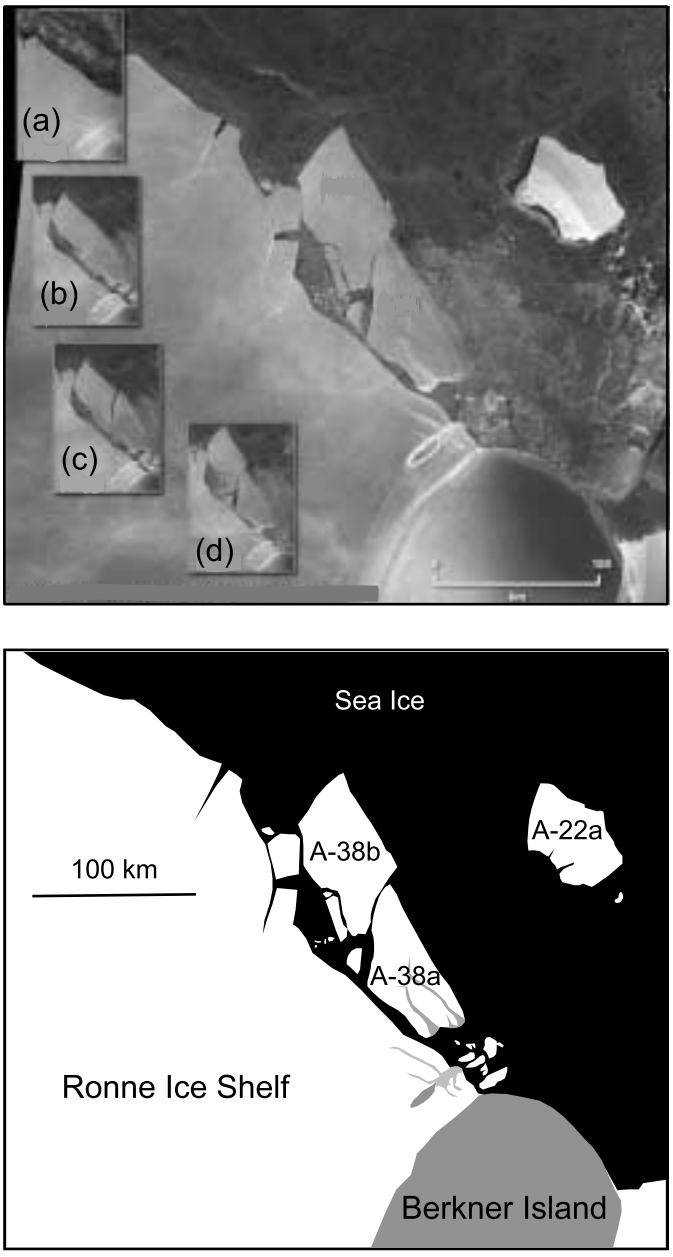

Figure 7. Radarsat SAR image of A38, A39 and A22 on November 1, 1998. Images for October 20, 22 and 27, 1998 are displayed as insets (b) - (d). Inset (a) displays the pre-calving configuration and shows large rifts that became detachment boundaries for A38. Radarsat imagery is provided courtesy of the Canadian Space Agency.

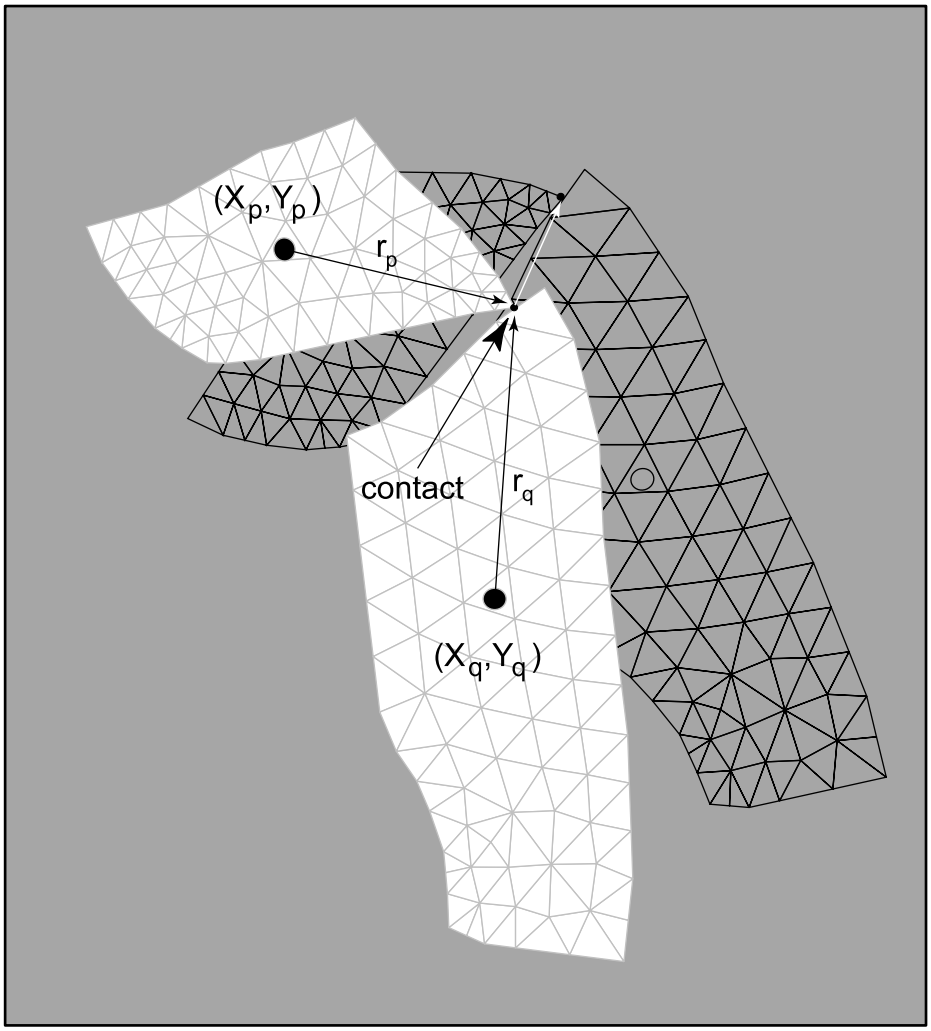

Figure 8. Geometry of two icebergs (A38a and A38b) in collision. Vectors $\vec{r}_p$ and $\vec{r}_q$ are shown for icebergs p and q that are in contact at one point. The centers of area of each iceberg are indicated by their Cartesian coordinates (X_p, Y_p) and (X_q, Y_q) on the polar stereographic projection of the Earth surface used in the model study. Also shown is the finite-element mesh used to compute forces and torques acting on each iceberg.

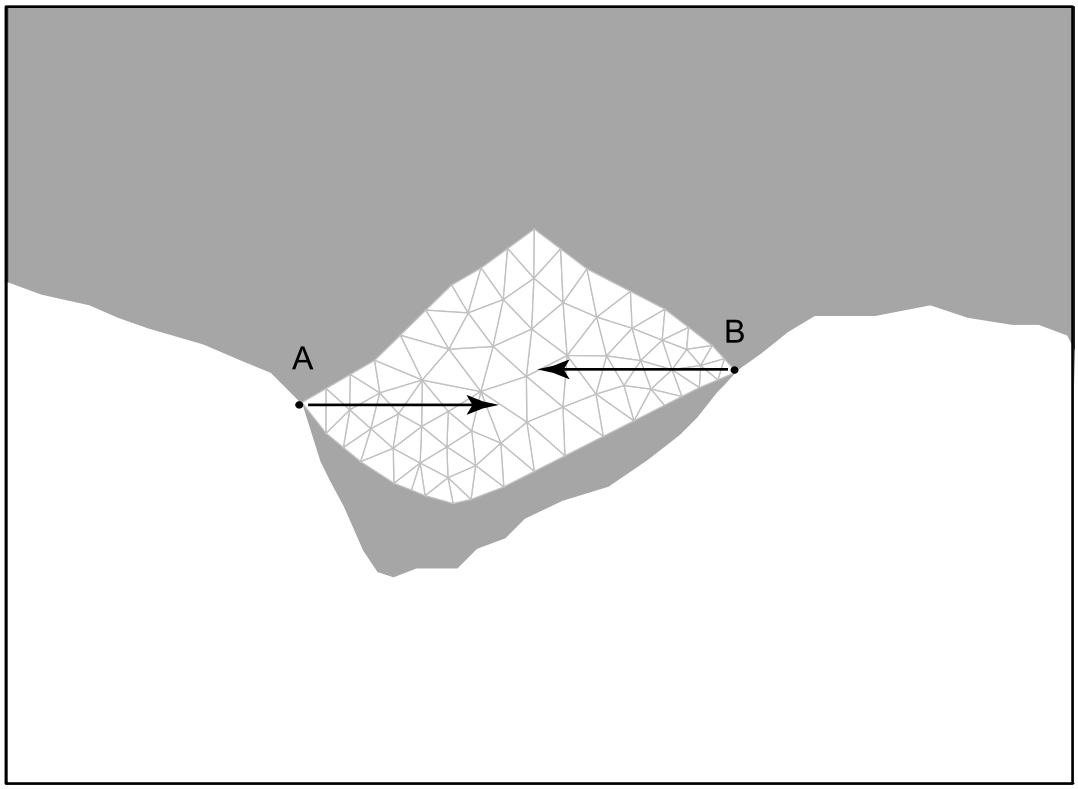

Figure 9. Schematic diagram of an iceberg (A38b) wedged in a V-shaped embayment of an idealized ice-shelf ice front. The iceberg cannot move until contact at point A or B is broken. During the time the iceberg is wedged, opposing forces of constraint, such as depicted by vectors emanating from points A and B, are not determined uniquely from the force balance of the iceberg. For simplicity, we use singular-value-decomposition to resolve such non-uniqueness.

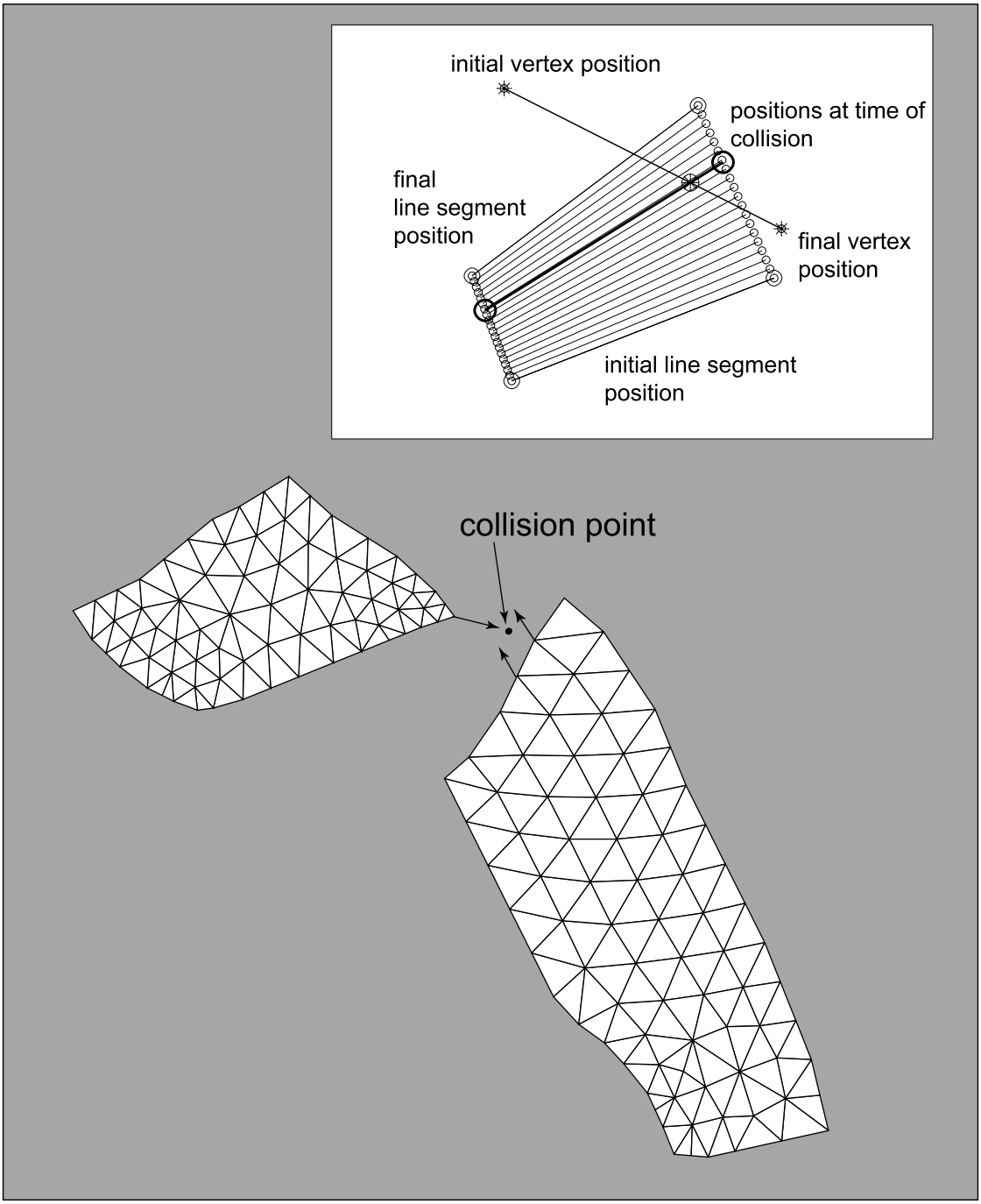

Figure 10. Schematic diagram of two icebergs (A38a and A38b) colliding. Inset: the geometry of vertex point and line segment computed through a single time step with the point of collision identified.

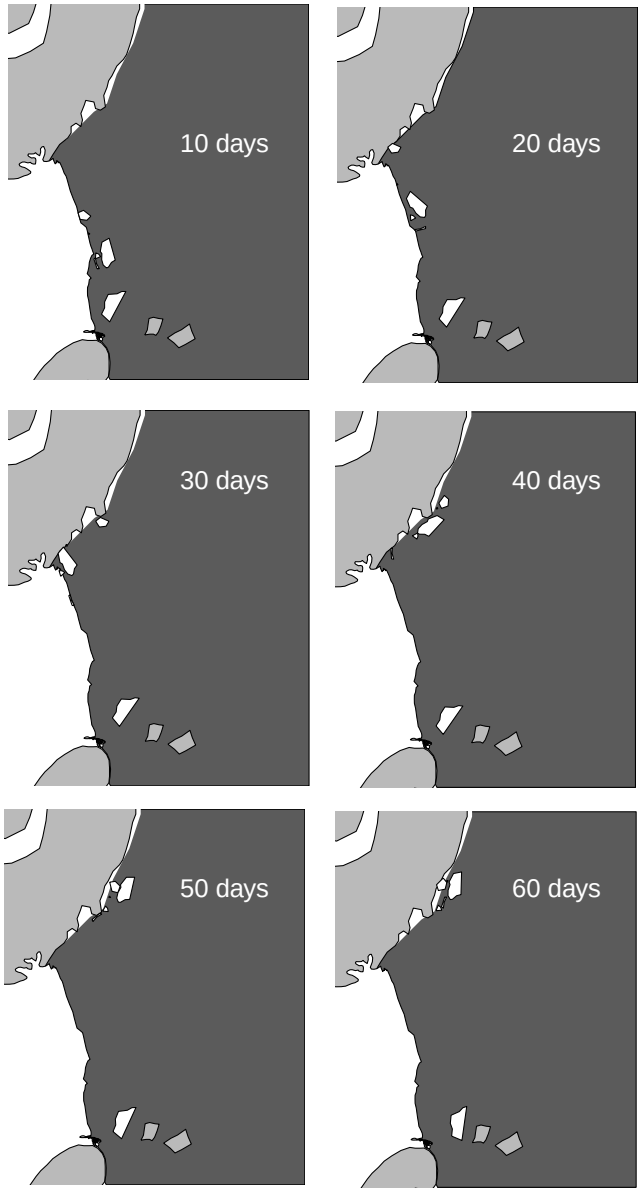

Figure 11. Drift of A38a, A38b, A39, and various other unnamed icebergs predicted by tide-forcing drift model. Total integration time is 60 days.

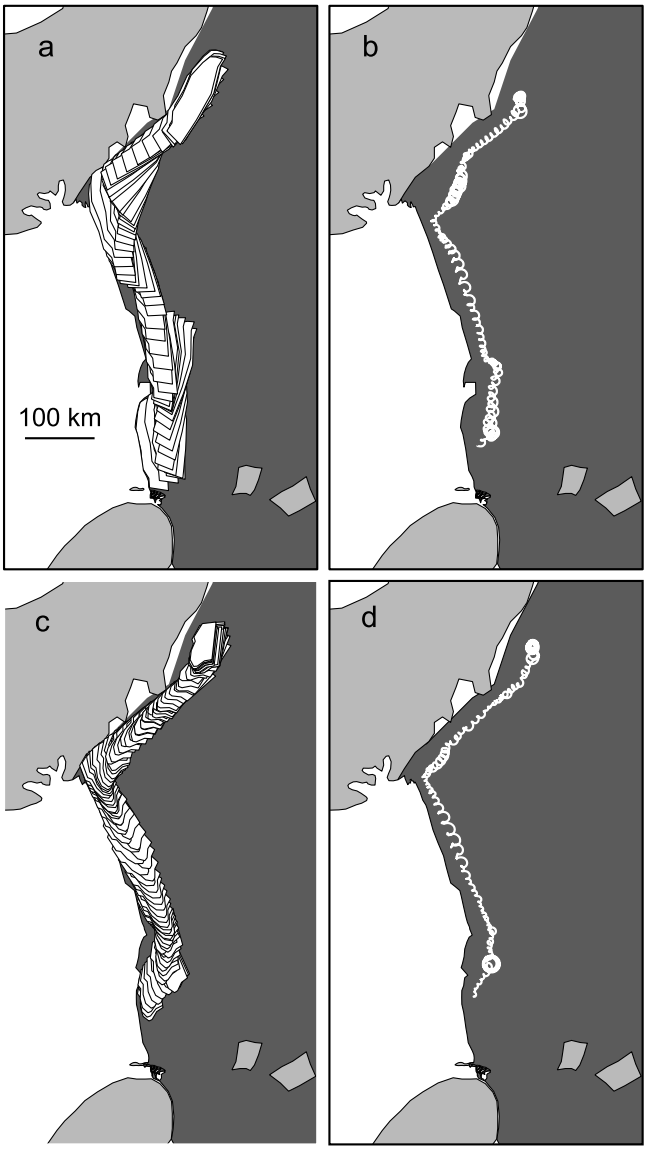

Figure 12. (a) and (b) Drift of A38 in its unbroken configuration computed with the model, for 60 days of integration. (c) and (d) Drift of A38b as a separate piece computed with the model, for 60 days of integration. The position of the iceberg is plotted every 24 hours in (a) and (c). The path of the iceberg's center of area, is shown in (b) and (d).

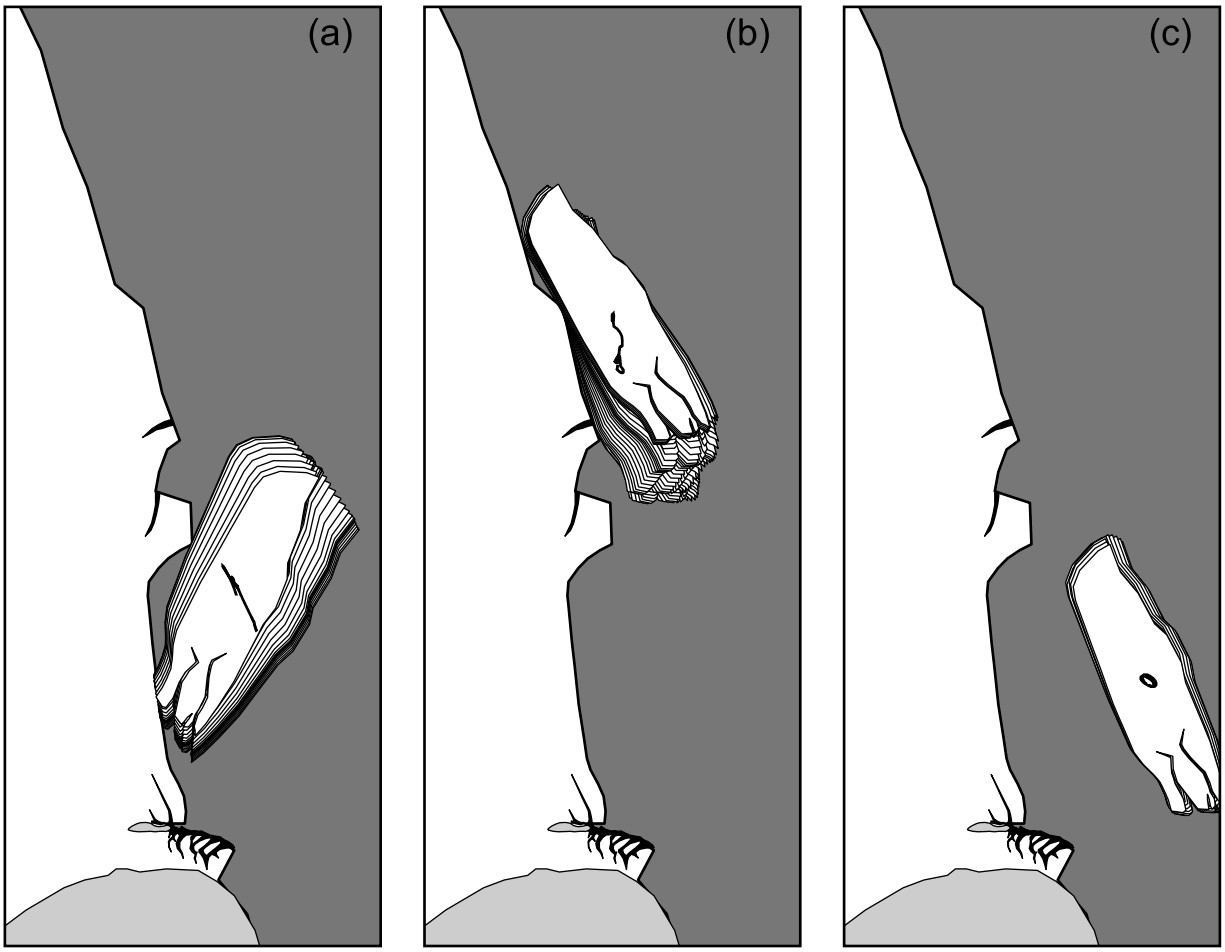

Figure 13. Simulated trajectories of A38 (as a single unbroken iceberg) during three 48-h drift simulations similar to that shown in Figure (11). Illustrations of (a) the iceberg colliding with a promontory on the ice front, (b) the iceberg rocking along the ice front (the kedging effect), and (c) the iceberg undergoing elliptical motion (when positioned in a manner so as to eliminate collisions with the ice front). The iceberg's positions are shown at hourly intervals.

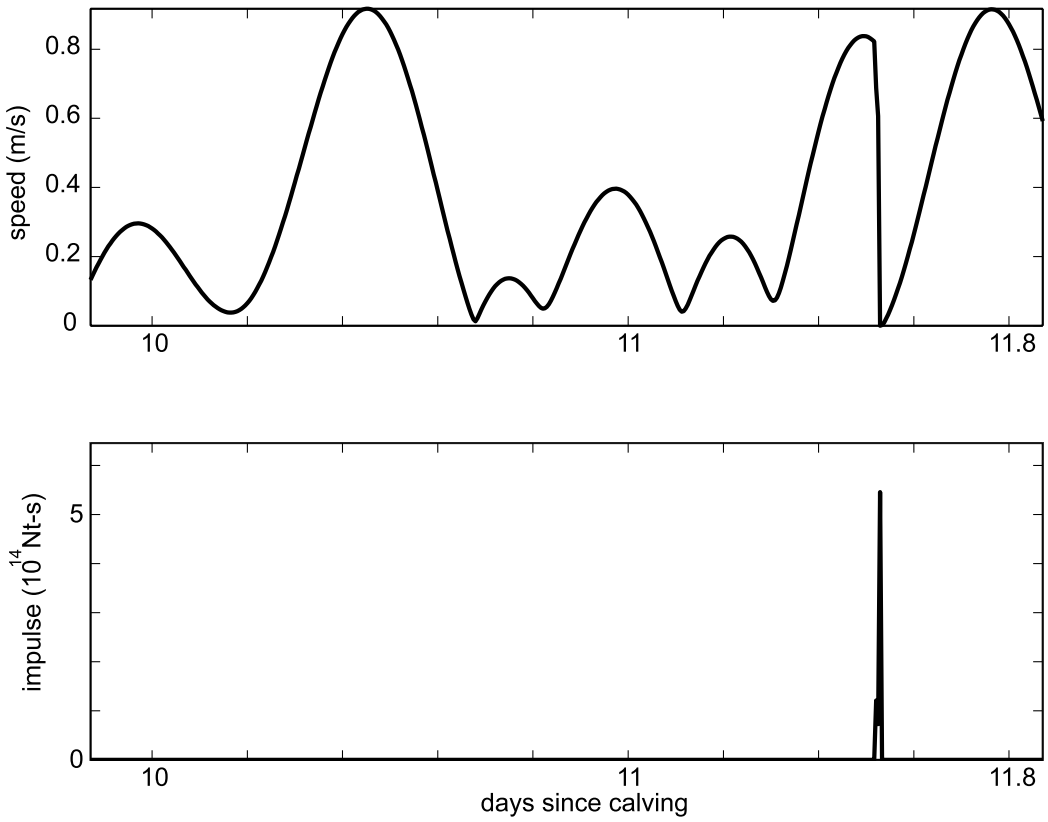

Figure 14. Speed (m s^{-1}), and impulse (net momentum change, 10^{14} Nt-s) associated with the ice-front collision shown in panel (a) of Figure (13).

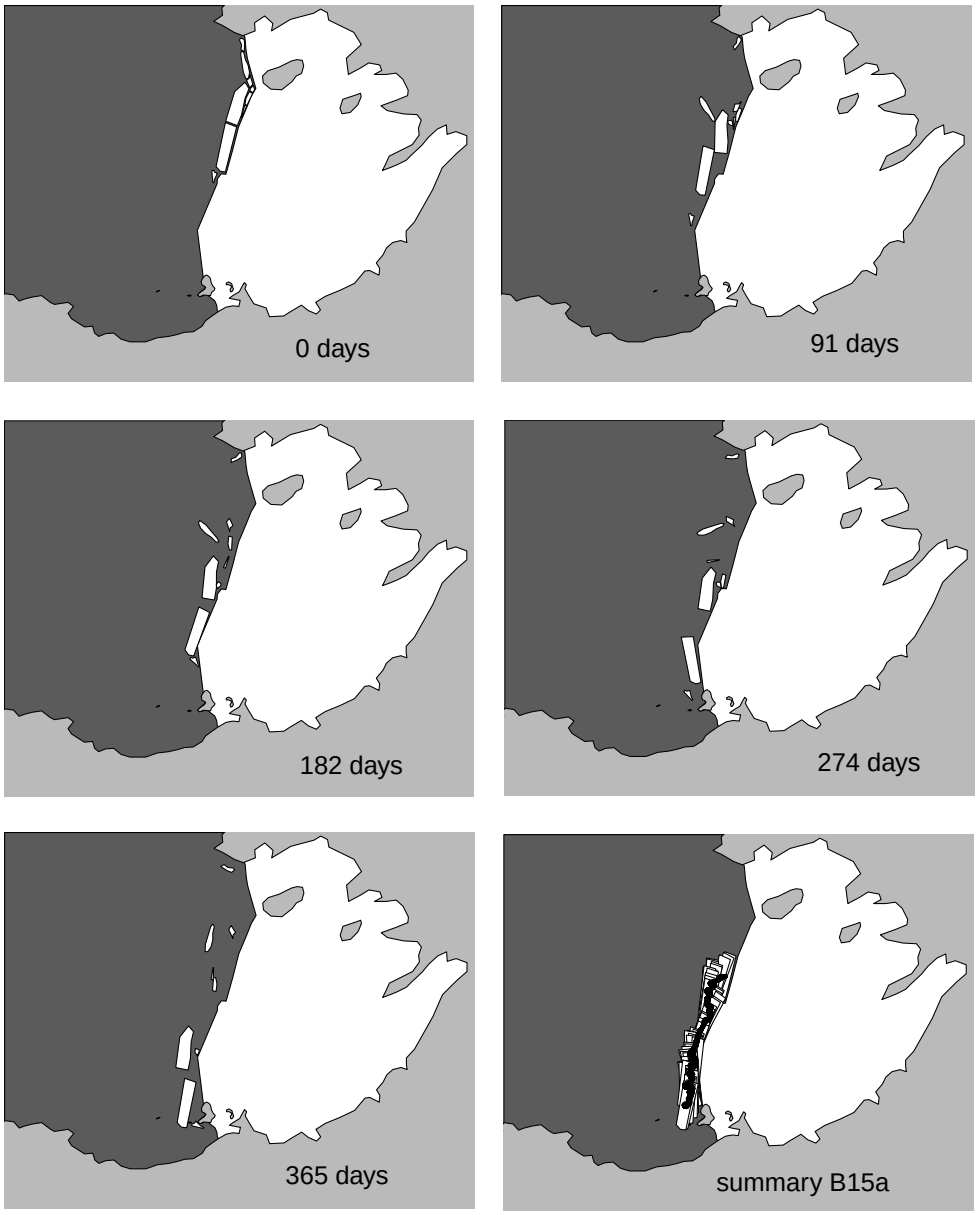

Figure 15. Drift of B15 - B18 predicted by tide-forcing drift model. The total integration time is 365 days.

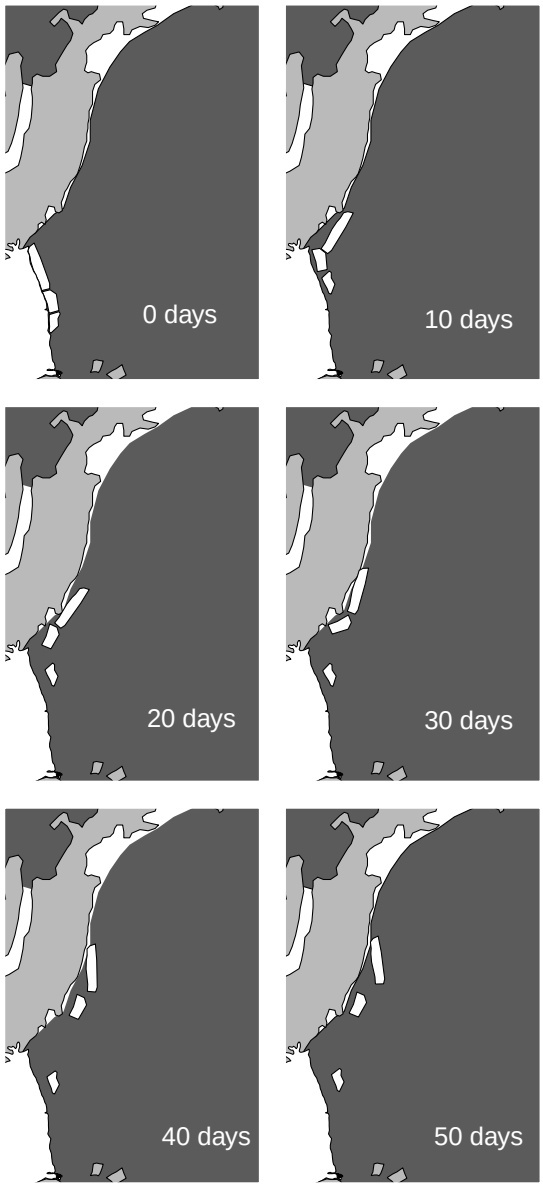

Figure 16. Drift of A43 and A44 predicted by tide-forcing drift model. The total integration time, 50 days, is shorter than that displayed in Figure (15) because tidal motions in the Weddell Sea are much stronger than in the Ross Sea.

Table 1. Approximate dimensions of icebergs considered in this study [following *Lazzara et al.,* 1999]. Length designates dimension of long axis.

Iceberg	Date	Length (km)	Width (km)
A38	October, 1998	166	46
A39	October, 1998	26	17
A43	May, 2000	257	36
A44	May, 2000	72	31
B15	March, 2000	295	37
B16	March, 2000	40	12
B17	April, 2000	89	18
B18	April, 2000	23	6